Water-CO_2-mineral systems: Interfacial tension, contact angle, and diffusion—Implications to CO_2 geological storage

D. Nicolas Espinoza[1] and J. Carlos Santamarina[1]

Received 10 September 2009; revised 27 February 2010; accepted 22 March 2010; published 29 July 2010.

[1] The interfacial interaction between mineral surfaces and immiscible fluids determines the efficiency of enhanced oil or gas recovery operations as well as our ability to inject and store CO_2 in geological formations. Previous studies have shown that the interfacial tension and contact angle in CO_2-water-mineral systems change noticeably with fluid pressure. We compile previous results and extend the scope of available data to include saline water, different substrates (quartz, calcite, oil-wet quartz, and polytetrafluoroethylene (PTFE)), and a wide pressure range (up to 20 MPa at 298K). Data analysis provides interfacial tension and contact angle as a function of fluid pressure; in addition, we recover the diffusion coefficient of water in liquid CO_2 from long-term observations. Results show that CO_2-water interfacial tension decreases significantly as pressure increases in agreement with previous studies. Contact angle varies with CO_2 pressure in all experiments in response to changes in CO_2-water interfacial tension: it increases on nonwetting surfaces such as PTFE and oil-wet quartz and slightly decreases in water-wet quartz and calcite surfaces. Water solubility and its high diffusivity ($D = 2 \times 10^{-8}$ to 2×10^{-7} m^2/s) in liquid CO_2 govern the evolution of interparticle pendular water. CO_2-derived ionic species interaction with the substrate leads to surface modification if reactions are favorable, e.g., calcite dissolution by carbonic acid and precipitation as water diffuses and migrates into the bulk CO_2. Pressure-dependent interfacial tension and contact angle affect injection patterns and breakthrough mechanisms, in other words, the performance of geological formations that act as either reservoirs or seals.

Citation: Espinoza, D. N., and J. C. Santamarina (2010), Water-CO_2-mineral systems: Interfacial tension, contact angle, and diffusion—Implications to CO_2 geological storage, *Water Resour. Res.*, *46*, W07537, doi:10.1029/2009WR008634.

1. Introduction

[2] Interfacial phenomena upscale through the sediment porous network to define multiphase flow characteristics. Thus, interfacial phenomena control enhanced oil and gas recovery [*Pope and Baviere*, 1991; *Rosen et al.*, 2005], methane production from hydrate bearing sediments [*Seo et al.*, 2002; *Sun et al.*, 2004; *Watanabe et al.*, 2005], and the ability to inject and store CO_2 in geological formations [*Chalbaud et al.*, 2009; *Chiquet et al.*, 2007; *Hildenbrand et al.*, 2004; *Plug and Bruining*, 2007; *Suekane et al.*, 2009]. Temperature and pressure vary considerably in these natural systems: from cold and relatively shallow permafrost and marine sediments (e.g., Alaska north slope: ~7 MPa, 278K) to warm coal seams (e.g., Alabama Black Warrior Basin: ~7 MPa, 296K) and deep hot rocks onshore (e.g., Weyburn oil field: ~14 MPa, 323K). Therefore, CO_2 can form a gas, liquid, or supercritical phase in various applications or environments.

[3] Interfacial tension arises at the molecular level as a result of van der Waals forces [*Butt et al.*, 2006; *Defay and Prigogine*, 1966]. Three interfacial tensions can be identified in a liquid (l), fluid (f), and solid substrate (s) system (Figure 1). While fluid-liquid interfacial tension σ_{fl} is directly measurable, fluid-solid σ_{fs} and liquid-solid σ_{ls} interfacial tensions are assessed through indirect methods [*Butt et al.*, 2006]. Foreign substances on the solid surface or within the fluids can modify any of the three interfacial tensions. The contact angle is influenced by other factors such as surface roughness, contact line fluctuations, vibrations, and viscous effects (see review by *Decker et al.* [1999]).

[4] The interfacial tension σ_{fl} between CO_2 ("fluid" implies either gas or liquid) and liquid water is susceptible to changes in temperature and pressure. At ~298K, the interfacial tension decreases from ~72 to 25 mN/m as pressure increases from 0.1 to 6.4 MPa, and it reaches a constant value ~30 mN/m after CO_2 liquefies (studies at 278–373K and up to 70 MPa can be found in the work of *Chun and Wilkinson* [1995], *Dickson et al.* [2006], *Kvamme et al.* [2007], *Massoudi and King* [1974a], and *Sutjiadi-Sia et al.* [2007]). Water salinity affects the interfacial tension between CO_2 and brine [*Chalbaud et al.*, 2009].

[5] The interfacial tension σ_{fs} between the solid substrate and CO_2 decreases significantly with the increase in CO_2 pressure for different substrates [*Dickson et al.*, 2006; *Sutjiadi-Sia et al.*, 2008]. For an increase in pressure (P = 0.1 to ~7 MPa), the corresponding decrease in σ_{fs} is 30 to ~0 mN/m in glass hydrophobized with dichlorodimethy-

[1]School of Civil and Environmental Engineering, Georgia Institute of Technology, Atlanta, Georgia, USA.

0043-1397/10/2009WR008634

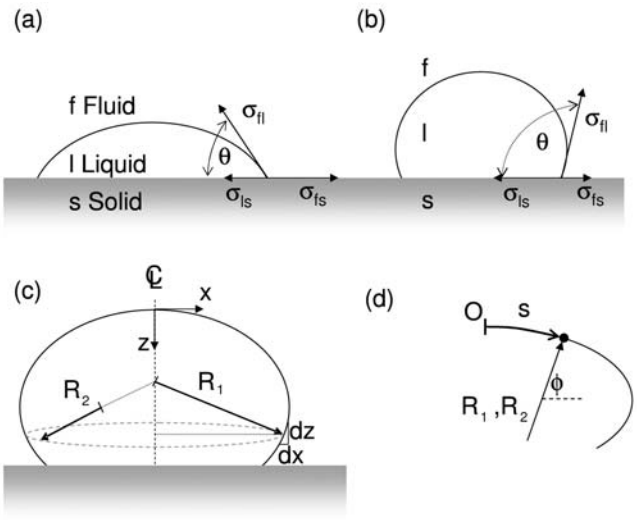

Figure 1. Contact angle: basic parameters in wettability. Components: surrounding fluid (f), liquid droplet (l), and solid substrate (s). (a) Partially wetting droplet. (b) Nonwetting droplet. Shape parameters in data reduction: (c) Cartesian coordinates system (x,z) and (d) coordinates along arc length (s,ϕ).

dilane, 24 to ~0 mN/m in polytetrafluoroethylene (PTFE), and 80–17 mN/m in glass.

[6] On the other hand, the interfacial tension σ_{ls} between water and the solid substrate remains relatively stable with the increase in fluid pressure; for example, the water-PTFE interfacial tension remains at $\sigma_{ls} \sim 25$ mN/m, for a pressure range between $P = 0.1$ and ~7 MPa [*Dickson et al.*, 2006]. Ionic species may interact with the solid substrate and alter σ_{ls}.

[7] The Young-Dupre equation relates the contact angle θ to the mutual interfacial tensions: $\cos\theta = (\sigma_{fs} - \sigma_{ls})/\sigma_{fl}$ (Figure 1). It follows that changes in interfacial tensions σ_{fl}, σ_{fs}, and σ_{ls} with CO_2 pressure alter the contact angle in water-CO_2-substrate systems. For an increase in pressure from $P = 0.1$ to ~8 MPa, the increase in contact angle is $\Delta\theta \approx$ 45° on glass hydrophobized with dichlorodimethydilane, $\Delta\theta \approx 50°$ on PTFE, $\Delta\theta \approx 15°$ on glass, $\Delta\theta \approx 25°$ on muscovite mica, and $\Delta\theta \approx 60°$ on coal [*Chi et al.*, 1988; *Chiquet et al.*, 2007; *Dickson et al.*, 2006; *Siemons et al.*, 2006; *Sutjiadi-Sia et al.*, 2007].

[8] The purpose of this manuscript is to extend the scope of previous studies summarized above to include other substrates and pore fluid conditions that may be encountered in natural systems, particularly in the context of CO_2 geological storage. We place emphasis on the simultaneous determination of interfacial tension and contact angle. We note that, while there is extensive data on the solubility and diffusivity of CO_2 in water, there is very limited information on the diffusivity of water in CO_2; therefore, we include complementary tests to evaluate molecular diffusion. Finally, we use experimental results to assess CO_2 injectability and storage in geological formations.

2. Device and Materials–Test Procedure–Data Reduction

2.1. Apparatus

[9] We use the sessile droplet method to determine the evolution in interfacial tension σ_{fl} and contact angle. This test configuration allows us to explore the effect of relative density from gas CO_2 to liquid CO_2 conditions. Tests are conducted within a stainless steel, high-pressure chamber, internal volume ~55cm^3, which has a sapphire window to allow for optical measurements (Figure 2a). The cell is instrumented with a pressure transducer (OMEGA PX303-GV) and a thermocouple (copper-constantan, Conax Buffalo) placed in the vicinity of the droplet. A fiber optic port provides internal illumination. Separate injection ports are available for CO_2 and water. The water droplet sits on the selected substrate at the center of the cell (Figure 2b).

2.2. Materials

[10] Water droplets involve either deionized water or brine prepared by mixing water with natural halite crystals at room temperature and atmospheric pressure. The tested

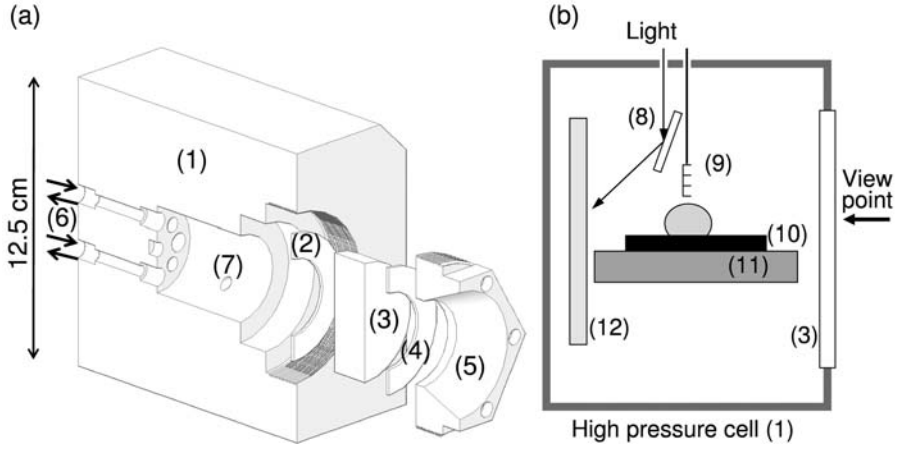

Figure 2. High-pressure chamber: (a) vertical cross section and (b) chamber detail. Components: (1) stainless steel body, (2) PTFE gasket, (3) sapphire window, (4) copper gasket, (5) screwable window fastener, (6) inlet-outlet fluid ports, (7) ports for transducers and illumination, (8) mirror, (9) length scale and thermocouple, (10) substrate, (11) stainless steel base, and (12) white light diffuser background.

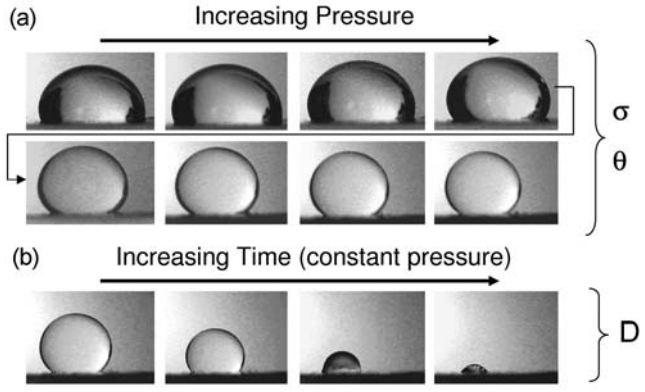

Figure 3. A water droplet on PTFE substrate surrounded by CO_2. (a) Changes in interfacial tension σ_{fl} and contact angle θ as CO_2 pressure increases from 0.1 to 18.5 MPa. (b) Size reduction as water diffuses into the surrounding liquid CO_2 (duration, ~400 min).

substrates include PTFE film, calcite crystal, clean glass (amorphous silica), and glass coated with oil (surface pretreated with toluene and *n*-heptane and coated with oil of medium viscosity from Maracaibo Lake reservoirs, procedure in the work of *Bryar and Knight* [2003]).

2.3. Test Procedure

[11] The chamber is first subjected to vacuum and gradually flushed with CO_2 (99.99% purity) to remove air. Then, we use a precision syringe to place a small water droplet (between 10 and 30 mm^3) on the horizontally resting substrate; such small droplets minimize gravitational effects and provide insight relevant to the scale of pendular water at interparticle contacts within sediments. The system is pressurized with CO_2 in stages, from an initial pressure of 0.1 MPa to a maximum pressure of 20 MPa. Temperature remains within 296.5 ± 1.5K at all times. We record the evolution of the droplet geometry using high-resolution time-lapse photography (3 μm pixel size). Figure 3 shows a typical sequence of images gathered during pressurization and during water diffusion into liquid CO_2. These images capture characteristic trends observed in most tests.

[12] We use images captured at stable temperature and pressure conditions to measure interfacial tension and contact angle, typically 8 min after each pressurization step. Although CO_2 diffuses quickly into the water at the interface, chemical equilibrium is not guaranteed and chemical reactions such as CO_2 speciation and calcite dissolution may continue during the test. Note that the water droplet consistently advances or recedes during pressurization.

2.4. Data Reduction: Interfacial Tension and Contact Angle

[13] Images are scaled and digitally processed to find the interface boundary using the Canny edge detection algorithm [*Canny*, 1986]. The CO_2-water interfacial tension σ_{fl}, curvature radii R_1 and R_2, and the pressure jump ΔP at any point on the interface are related by Laplace's equation [*Blokhuis*, 2004; *Rotenberg et al.*, 1983],

$$\sigma_{fl}\left(\frac{1}{R_1}+\frac{1}{R_2}\right)=\Delta P. \tag{1}$$

Gravity g and the difference in density $\Delta\rho$ between water or brine and CO_2 cause a pressure gradient $\Delta\rho gz$ along the droplet height. Let us consider cartesian coordinates (x,z) measured from the droplet apex (see Figure 1c) and a parametrized representation of the interface based on the curve length s (Figure 1d), then

$$\frac{dx}{ds}=\cos\phi \quad \text{and} \quad \frac{dz}{ds}=\sin\phi. \tag{2}$$

Since curvature radii are $1/R_1 = d\phi/ds$ and $R_2 = x/\sin\phi$, equation (1) can be rewritten as

$$\sigma_{fl}\left(\frac{d\phi}{ds}+\frac{\sin\phi}{x}\right)=\frac{2\sigma_{fl}}{R_0}+\Delta\rho\, gz, \tag{3}$$

where R_0 is the curvature at the droplet apex. The recorded droplet profile permits recovering local values of ϕ, s, z everywhere and measuring R_0 at the apex. The difference in mass densities $\Delta\rho$ is computed from equations of state. For water density, we use expressions in the works of *Perry and Green* [1997] and *McCutcheon et al.* [1993]; we do not correct for minor changes in water density associated with CO_2 dissolution. For CO_2, we consider it as a pure phase and compute its density using the equation in the work of *Duan and Sun* [2003].

[14] The only remaining unknown in equation (3) is the interfacial tension σ_{fl}. We choose to simultaneously fit a large number of points (x,z) to increase accuracy. We digitize the complete droplet profile (1000–6000 points) and fit the points with the lowest-degree polynomial that properly justifies the data; typically a degree 3–5 suffices. Contact angle θ (tangent when coordinates correspond to the substrate position), droplet volume, and surface area are calculated from the fitted polynomial assuming axisymmetry. Interfacial tension is obtained by minimizing the L^2 norm $E = \Sigma\varepsilon_i^2$ of individual errors in pressure ε_i at each point along the droplet profile, where ε_i is the difference between the pressure predicted with local curvatures $\sigma_{fl}(1/R_1 + 1/R_2)$ and the pressure as a function of depth z from the apex $(2\sigma_{fl}/R_0 + \Delta\rho gz)$. All calculations are repeated for both left and right halves of the droplet. This data-intensive measurement method gives consistent results, and the estimated error is $\Delta\sigma = \pm 2.5$ mN/m for interfacial tension and $\Delta\theta = \pm 0.6°$ for contact angle.

2.5. Data Reduction: Diffusion

[15] Water diffuses into the surrounding CO_2 until the two phases equilibrate. The instantaneous droplet volume and surface area allow us to evaluate the rate of water diffusion into the surrounding CO_2 medium. The diffusion coefficient D is inverted from successive forward simulations of the diffusion equation in terms of the concentration c of water in liquid CO_2, radial coordinates r, and time t,

$$\frac{\partial c}{\partial t}=D\left(\frac{2}{r}\frac{\partial c}{\partial r}+\frac{\partial^2 c}{\partial r^2}\right). \tag{4}$$

We estimate the droplet volume and initial droplet equivalent radius R from the droplet shape. The injected liquid CO_2 is water free, therefore $c(r > R, t = 0) = 0$. Even though the water droplet decreases in size, we assume that water dissolved in the space previously occupied by the con-

Table 1. Scope of the Experimental Study[a]

Gas	Droplet Liquid	Substrate	σ_{fl}	θ	D
CO_2	H_2O	$CaCO_3$	NA	3	–
		PTFE	3	3	1
		Amorphous SiO_2	NA	1	–
		Oil-wet SiO_2	3	3	2
	Brine	$CaCO_3$	NA	1	–
		PTFE	2	2	1
		Amorphous SiO_2	NA	1	–

[a]Numbers in the table indicate the number of independent tests conducted for each condition.

tracting droplet is negligible, and consequently the concentration c of water in liquid CO_2 at a distance equal to the droplet original radius is constant and equal to the solubility limit at that particular pressure and temperature $c(r = R,t) = C_0$. Because the water droplet is placed within a closed system size r_b, there is no flux through the boundaries and the spatial derivative is $\partial c/\partial r|_{r = r_b} = 0$ at the chamber walls. The reaction $H_2O + CO_2 \rightarrow H_2CO_3$ and further speciation are assumed to be much faster than the diffusion time.

3. Results and Analyses

[16] Table 1 shows tests conditions explored in this study. Experiments are designed to achieve high measurement precision and to improve invertibility of unknown parameters. In particular, interfacial tension cannot be properly resolved when the contact angle θ is <80° and the droplet is flat, so emphasis is placed on nonwetting substrates when interfacial tension data are sought. The liquid CO_2 is presaturated with water to prevent water diffusion and to improve interfacial tension measurements in long duration tests. Experimental results and related analyses are presented next for the three parameters studied in this research: interfacial tension, contact angle, and water diffusion in liquid CO_2.

3.1. Interfacial Tension

[17] Figure 4 shows the measured interfacial tension σ_{fl} between CO_2 and water as a function of pressure; data compiled from the literature are shown as well. Interfacial tension decreases as CO_2 pressure increases, and it remains constant once the CO_2 vapor-liquid boundary is reached (~6.43 MPa at 298K). Three sets of experiments are identified:

[18] 1. Deionized water droplets (solid circles in Figure 4): Our results are in agreement with previous studies [*Chun and Wilkinson*, 1995; *Kvamme et al.*, 2007; *Massoudi and King*, 1974a; *Sutjiadi-Sia et al.*, 2007]. The interfacial tension between CO_2 and water σ_{fl} starts at ~72 mN/m at 0.1 MPa and 295K and decreases linearly at a rate of ~7 mN/m per MPa increase in CO_2 pressure until the liquid-vapor boundary is reached. Thereafter, the interfacial tension remains nearly constant at $\sigma_{fl} \approx$ 20–30 mN/m. (Note: *Kvamme et al.* [2007] observed a smooth transition in the supercritical regime.)

[19] 2. Brine droplets (open diamonds in Figure 4): The interfacial tension σ_{fl} between CO_2 and brine is higher than between CO_2 and deionized water, and it exhibits lower sensitivity to pressure. (Note: higher pressure sensitivity has been observed in the supercritical regime at significantly higher temperatures [*Chalbaud et al.*, 2009].)

[20] 3. Water droplets with organic compounds that dissolved from the substrate (crosses in Figure 4): The CO_2-water interfacial tension σ_{fl} is lower than for deionized water without organic contaminants, but rates of decrease with pressure are the same (in agreement with data from the work of *Chun and Wilkinson* [1995]).

[21] Overall, values of CO_2-water interfacial tension can vary by ±10 mN/m, depending on the dissolved compounds in water.

[22] These results are the consequence of molecular interaction taking place within the liquid and between water and the surrounding CO_2.

3.1.1. Interactions Within the Liquid

[23] Foreign species modify the local electrical field within the liquid. Variations in interfacial tension σ (mN/m) with solute concentration c (mol/L) are anticipated in terms of surface excess of solute Γ (mol·m^{-2}) [*Butt et al.*, 2006; *Pegram and Record*, 2007; *Tuckermann*, 2007],

$$\left.\frac{\partial \sigma}{\partial(\gamma c)}\right|_T = -\frac{RT}{\gamma c}\Gamma, \tag{5}$$

where γ (dimensionless) is the solute activity coefficient and T (K) is temperature. In agreement with this theory, ions are depleted at the interface $\Gamma < 0$ in inorganic solutions, but there is enrichment of organic species $\Gamma > 0$ at the interface when organic compounds are present. In the case of CO_2, there is high concentration of dissolved CO_2 near the interface ($\Gamma > 0$), causing the observed drop in interfacial tension [*Chun and Wilkinson*, 1995; *Massoudi and King*, 1974b; *Sutjiadi-Sia et al.*, 2008]. Gibbs' isotherms $\Gamma = f(\gamma c)$ give insight into molecular mechanisms responsible for adsorption at the interface and differences among gases [*Massoudi and King*, 1974a]. Molecular dynamics simulations show the preferential alignment of water molecules near interface ions [*Bhatt et al.*, 2004] and of water and CO_2

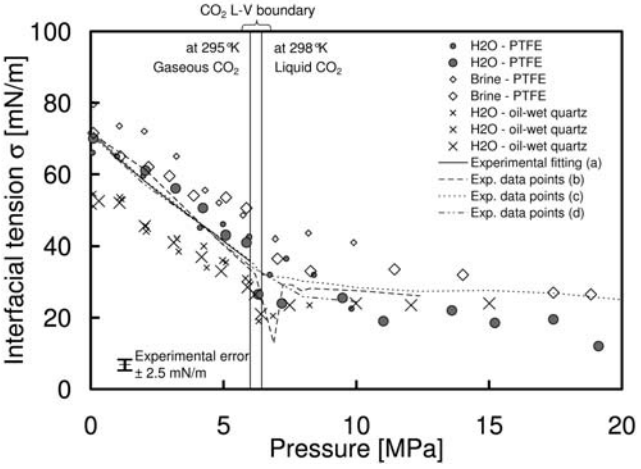

Figure 4. Interfacial tension between water and CO_2. Lines indicate values reported in the literature for deionized water at ~298K [a, *Massoudi and King*, 1974b; b, *Chun and Wilkinson*, 1995; c, *Kvamme et al.*, 2007; d, *Sutjiadi-Sia et al.*, 2007]. Note: the salt concentration in brine is ~200 g (NaCl)/kg(water).

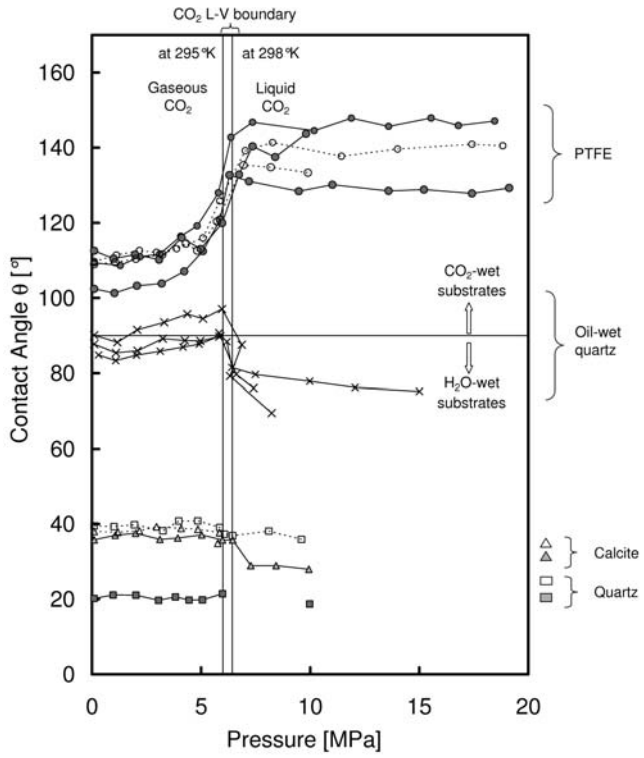

Figure 5. Contact angle evolution with pressure for a water droplet surrounded by CO_2 and resting on hydrophobic substrates (oil-wet quartz and PTFE) and hydrophilic substrates (quartz and calcite). Continuous line, deionized water; dashed lines, brine ~200 g(NaCl)/kg(water).

molecules at the interface [*da Rocha et al.*, 2001; *Kuznetsova and Kvamme*, 2002; *Kvamme et al.*, 2007].

3.1.2. Interaction With the Surrounding Fluid

[24] The proximity to and the number of near-neighbor charges in the surrounding fluid depends on the difference between fluid densities. Hence, higher interaction and lower interfacial tension are expected with increasing CO_2 pressure and density, as suggested by the Sugden-Macleod equation $\sigma = f(\Delta\rho)$ [*Chalbaud et al.*, 2009; *Chun and Wilkinson*, 1995]. Consequently, the interaction with the external fluid and the value of σ_{fl} remain relatively constant once the pressure exceeds the vapor-liquid boundary.

3.2. Contact Angle

[25] Figure 5 shows the evolution of contact angle θ with pressure for all substrates. The following can be observed:

[26] 1. The contact angle on nonwetting PTFE substrates increases (from 100° to 140°), as pressure increases and remains almost constant after the pressure exceeds the liquid-vapor interface.

[27] 2. The contact angle on oil-wet silica increases slightly (from 85° to 90°) when CO_2 pressure increases from 0.1 MPa to the pressure at the liquid-vapor boundary ~6.43 MPa at 298K; thus, this substrate can turn from slightly hydrophilic to hydrophobic upon pressurization. At any given pressure, contact angles are similar for brine and deionized water.

[28] 3. Contact angles on amorphous silica SiO_2 and calcite $CaCO_3$ substrates remain nearly constant with pressure. Dissolved NaCl in water increases the contact angle by ~20° for brine on SiO_2 and ~4° for brine on $CaCO_3$.

[29] 4. Published results for glass, PTFE, and coal substrates are similar to those obtained in this study [*Chi et al.*, 1988; *Dickson et al.*, 2006; *Sutjiadi-Sia et al.*, 2007].

[30] Our results also show that contact angles between (1) liquid-CO_2 and water and (2) liquid-CO_2 and all tested solid substrates ($CaCO_3$, oil-wet SiO_2, and PTFE) approach $\theta \approx 0$ in a vapor-CO_2 atmosphere.

[31] Let us consider the Young-Dupre's equation in differential form to identify the influence that changes in each component exert on $\cos\theta$ upon small changes in gas pressure,

$$\frac{d(\cos\theta)}{dP} = -\frac{\sigma_{fs} - \sigma_{ls}}{\sigma_{fl}^2}\frac{\partial\sigma_{fl}}{\partial P} + \frac{1}{\sigma_{fl}}\frac{\partial\sigma_{fs}}{\partial P} - \frac{1}{\sigma_{fl}}\frac{\partial\sigma_{ls}}{\partial P}. \quad (6)$$

This expression explains changes in contact angle reported in Figure 5:

[32] 1. On hydrophobic substrates (PTFE and oil-wet quartz): A reduction in $\sigma_{fl} = \sigma_{CO_2\text{-}H_2O}$ combines with a decrease in $\sigma_{fs} = \sigma_{CO_2\text{-substrate}}$ (reported in the literature) to cause an increase in contact angle with pressure.

[33] 2. On hydrophilic quartz and calcite: The addition of NaCl increases $\sigma_{fl} = \sigma_{CO_2\text{-}H_2O}$ and results in a higher contact angle. On the other hand, the decrease in $\sigma_{fl} = \sigma_{CO_2\text{-}H_2O}$ is partially compensated by a decrease in $\sigma_{fs} = \sigma_{CO_2\text{-substrate}}$ (not observed explicitly), and the contact angle remains relatively unchanged.

[34] The observed contact angle $\theta \approx 0°$ for liquid CO_2-substrate in vapor CO_2 atmosphere is in agreement with the reported $\sigma_{CO_2(vapor)\text{-}CO_2(liquid)} \approx 0$.

3.3. Water Diffusion in Liquid CO_2

[35] The decrease in droplet volume with time observed in Figure 3 was measured for several conditions. We inverted for the diffusion coefficient D of water in liquid CO_2 using the procedure outlined earlier; results are summarized in Figure 6. The water solubility in liquid CO_2 was assumed to vary from 1.05 kg/m^3 at 10 MPa to 2.1 kg/m^3 at 25 MPa (measurements at 298–303K [*Chrastil*, 1982; *Jackson et al.*, 1995; *Sabirzyanov et al.*, 2002; *Spycher et al.*, 2003; *Wiebe*, 1941]). Our measured values and previously reported data are plotted in Figure 7:

[36] 1. Previously published NMR experiments D = from 1.5×10^{-8} to 2×10^{-8} m^2/s at 298K, 13–20 MPa [*Xu et al.*, 2003] and molecular simulations D = from 16×10^{-8} to 2×10^{-8} m^2/s at 308.9K, 6.3–17.1 MPa [*Danten et al.*, 2005].

[37] 2. In our measurements, uncertainty in the solubility of water in CO_2 is responsible for an estimation error of $\varepsilon \approx \pm 4 \times 10^{-8}$ m^2/s.

[38] 3. Values range from $D = 1.2 \times 10^{-7}$ to 1.8×10^{-7}m^2/s for water to $D = 1.0 \times 10^{-7}$m^2/s for brine. The lower diffusion coefficient for brine reflects the attraction of water to ions in the aqueous solution. In fact, we observe salt precipitation as water molecules leave the droplet and migrate into the bulk liquid CO_2.

[39] 4. The measured diffusion of water in liquid CO_2 is much faster than the diffusion of CO_2 in water $D = 2 \times 10^{-9}$–5×10^{-9} m^2/s [*Thomas and Adams*, 1965], ions in water $D \sim 10^{-9}$ m^2/s [*Sharma and Reddy*, 2001], and

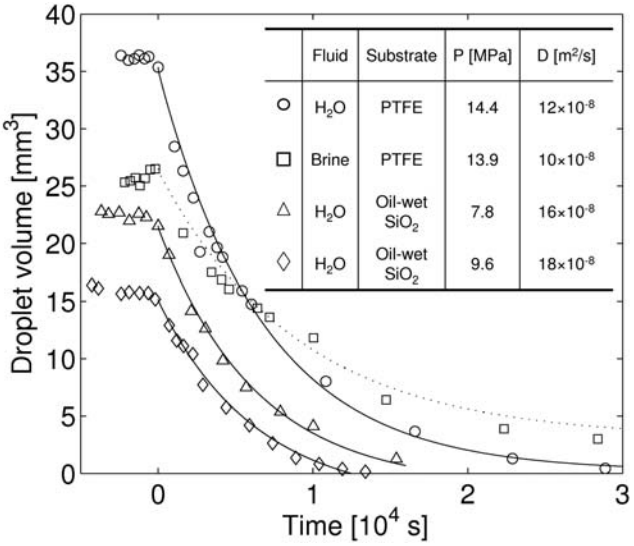

Figure 6. Water diffusion in liquid CO_2. Change in droplet volume with time. Lines represent the best fit using the diffusion model, i.e., equation (4).

organic compounds in supercritical CO_2 $D = 2 \times 10^{-8}$–1×10^{-8} m^2/s (experiments at 313K [*Funazukuri et al.*, 1992; *Liong et al.*, 1992; *Sassiat et al.*, 1987]).

[40] 5. A decrease in D with pressure is apparent.

[41] We corroborated our droplet-based results by means of a 1-D configuration using a capillary tube to create a steady state diffusion condition (data also shown in Figure 7). Values inverted from droplet tests are approximately twice higher from the 1-D steady state experiment $D = 6.0 \times 10^{-8}$ m^2/s (probably due to convective currents). Nevertheless, all our experiments confirm the very high diffusivity of water in liquid CO_2.

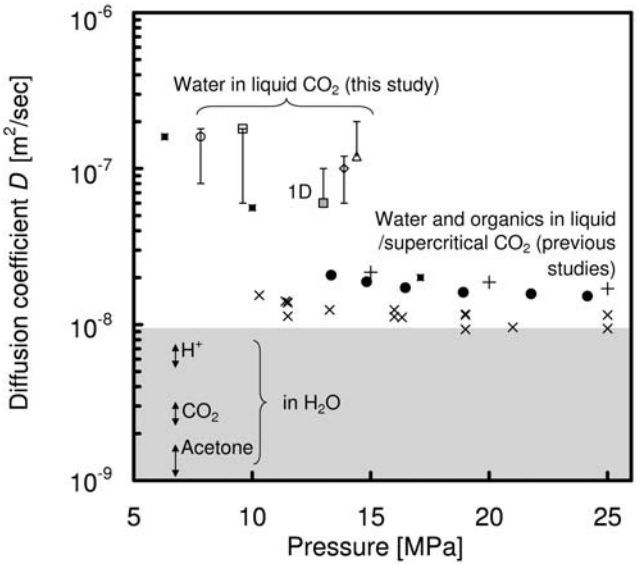

Figure 7. Water diffusion in liquid CO_2. Open symbols represent our experiments (296.5 ± 1.5K, the shaded square corresponds to the 1D tube). Literature data for diffusion coefficients: (1) water in liquid and supercritical CO_2 (small squares [298K, *Xu et al.*, 2003] and circles [308.9 and 313.9K, *Danten et al.*, 2005]); (2) CO_2 in supercritical CO_2 (+) [313.16K, *Suarez-Iglesias et al.*, 2008]; and (3) benzene, naphthalene, acetone, and ester in supercritical CO_2 (×) [313K, *Funazukuri et al.*, 1992; *Liong et al.*, 1992; *Sassiat et al.*, 1987]. The water diffusion coefficients for species dissolved in water are relatively insensitive to pressure (shaded area [~298K, *Krynicki et al.*, 1978]).

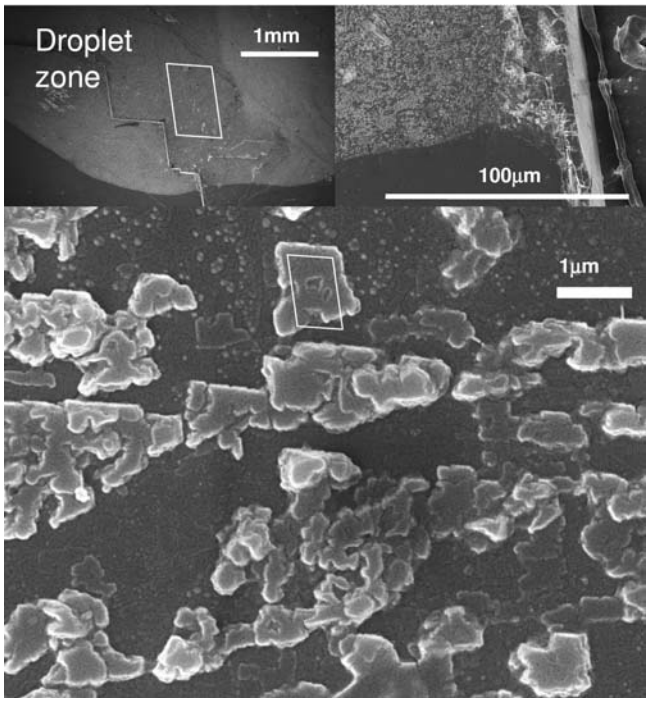

Figure 8. Precipitated calcite observed underneath the initial location of the water droplet after evaporation. Dissolution was caused by CO_2 acidification of water in the droplet.

[42] The high diffusivity of water in liquid CO_2 is attributed to the small size of water molecules in terms of equivalent molecular radius and the low viscosity of liquid CO_2, μ_{CO_2}. Note: μ_{CO_2} increases with pressure and decreases with temperature; values range from 2×10^{-5} Pa·s at 5 MPa and 318K to 10^{-4} Pa·s at 30 MPa and 298K [*Fenghour et al.*, 1998].

3.4. CO_2-H_2O-Substrate Chemical Reactions

[43] We witness mineral corrosion during these tests. Furthermore, we also observed the reprecipitation of calcite in the form of typical trigonal-rhombic crystals on the mineral surface after water evaporation or water diffusion out of the droplet. SEM images are shown in Figure 8. Similar micron-size precipitated crystals are reported for calcite precipitation from calcium slurry [*Montes-Hernandez et al.*, 2007]. Note: bicarbonate may precipitate as aragonite if temperature exceeds $T > 303$K [*Cowan and Weintritt*, 1976].

[44] The presence of CO_2 changes the chemistry of the water droplet. Carbon dioxide dissolves in water with a solubility that depends on pressure and temperature ("aq" stands for aqueous form),

$$CO_2(\text{g-or-l}) \leftrightarrow CO_2(\text{aq}),$$

$$H_2O(\text{l}) + CO_2(\text{aq}) \leftrightarrow H_2CO_3(\text{aq}) \text{ carbonic acid.}$$

Table 2. Carbon Dioxide Solubility and Aqueous Species Concentration at Equilibrium Under CO_2 Pressure With and Without $CaCO_3$[a]

CO_2 Pressure (MPa)	Solubility of CO_2 in Water at 298.15K (mol/L)	Equilibrium (pH)	Concentration (mol/L)		
			$H_2CO_3^0$	HCO_3^-	Ca^{2+}
In the Absence of $CaCO_3$					
$10^{-4.5}$	$\sim 10^{-5}$	5.65	10^{-5}	$10^{-5.5}$	
0.1	0.0325	3.92	0.027	1.21×10^{-4}	
6.4	1.376	3.09	1.14	8.14×10^{-4}	
10	1.421	3.07	1.18	8.14×10^{-4}	
20	1.559	3.05	1.29	8.83×10^{-4}	
In the Presence of $CaCO_3$					
6.4	1.376[b]	4.85	1.14	0.047	0.023
10	1.421[b]	4.83	1.18	0.048	0.024
20	1.559[b]	4.79	1.29	0.054	0.027

[a]Temperature = 298K. CO_3^{-2} concentration is negligible. The SUPCRT92 thermodynamic data base is used for high-pressure calculations [*Johnson et al.*, 1992]. CO_2 solubility obtained from the work of *Duan and Sun* [2003].

[b]Assumption: CO_2 solubility in water is not significantly affected by Ca^{2+} concentration.

Carbonic acid ionizes stepwise to produce bicarbonate and carbonate ions,

$$H_2CO_3(aq) \leftrightarrow H^+(aq) + HCO_3^-(aq),$$

$$HCO_3^-(aq) \leftrightarrow H^+(aq) + CO_3^{2-}(aq).$$

Table 2 shows the concentration of these species at different pressures obtained from thermodynamic equations. The increase in CO_2 pressure results in both higher solubility of CO_2 and higher concentration of aqueous species. Reactions occur in the order of seconds for carbon hydration $d[CO_2]/dt \sim 0.03\ s^{-1}\ [CO_2]$ (brackets mean concentration in mol/L) and it is even faster for stepwise ionization [*Stumm and Morgan*, 1996]. Therefore, the availability of species within the droplet is diffusion limited in real systems size L where the characteristic diffusion time is on the order of L^2/D.

[45] Calcite $CaCO_3$ experiences relatively fast reactions with water acidified by CO_2,

$$CaCO_3(s) + H_2O + CO_2(g) \leftrightarrow Ca^{2+} + 2{\cdot}HCO_3^-.$$

Dissolution rates are proportional to the pH difference with respect to the equilibrium condition, and aqueous species are produced proportionally to the CO_2 pressure increase [*Drever*, 1997]. Conversely, a reduction in CO_2 pressure produces nucleation of CO_2 in gaseous form and the precipitation of calcite. $CaCO_3$(s) buffering and dissolution causes a ~2 orders of magnitude increase in HCO_3^-, as compared with the nonreactive case. Both chemical analyses of $CaCO_3$ dissolution and the estimated volume of precipitates in SEM images (thickness assumed ~0.3 μm) provide similar mass estimates.

4. Discussion: Implications to CO_2 Geological Storage

[46] Interfacial tension and contact angle define interparticle capillary forces, the capillary strengthening of the granular skeleton, and irreducible saturation or capillary trapping. In turn, pore scale and grain scale effects determine the thermo-hydro-chemo-mechanical coupled response of the geological formation. Injectability and seal performance are considered next in view of experimental results obtained in this study.

4.1. CO_2 Injectability

[47] The displacement of the saturating brine by liquid CO_2 depends on their viscosities μ_{CO_2} and μ_{brine}, the pore flow velocity v and capillary resistance at pore throats. Let us consider a pore as a cylindrical tube length L going from node i to node j. The equilibrium condition when liquid CO_2 displaces brine along the tube is given by

$$P_i = P_j + 4\frac{\sigma\cos\theta}{d} + v\frac{32L}{d^2}\left(\frac{l_{CO_2}\mu_{CO_2} + l_{brine}\mu_{brine}}{L}\right), \quad (7)$$

where the second term is Laplace's equation and the third term is Poiseuille's equation. Therefore, wettability (e.g., $\sigma\cos\theta > 0$, if the host fluid is the wetting one) and viscous drag determine imbibition and the occupancy of pores by either the wetting or the nonwetting fluid. The balance between participating forces can be captured in two dimensionless ratios: between viscous components M and between viscous and capillary forces C,

$$M = \frac{\mu_{CO_2}}{\mu_{brine}} \quad \text{and} \quad C = \frac{v\mu_{CO_2}}{\sigma\cos\theta}. \quad (8)$$

Values of viscosity $\mu_{brine} = (1 \pm 0.5) \times 10^{-3}$ Pa·s at 323K and $\mu_{CO_2} = (2{-}8) \times 10^{-5}$ Pa·s at 318K and from 5 to 30 MPa [*Fenghour et al.*, 1998; *Netherton et al.*, 1977], readily show that that the viscosity number is low for liquid CO_2-brine systems $M = \mu_{CO_2}/\mu_{brine} \sim 10^{-2}$. On the other hand, the C ratio varies with distance to the injection well and pressure-dependent σ and θ values.

[48] Different invasion patterns develop as a function of M and C [*Lenormand et al.*, 1988; *Pennell et al.*, 1996]. We can anticipate the following situations developing during liquid CO_2 injection into the reservoir:

[49] 1. Near the injection well, high flow velocity (high C-low M): Viscosity controls the invasion of CO_2 into the formation. Given the low viscosity number M for liquid CO_2-brine systems, liquid CO_2 will preferentially displace brine from the largest pores, but it will be prone to instability and viscous fingering may emerge [*Lenormand et al.*, 1988].

[50] 2. Far from the injection well, low flow velocity ($v \rightarrow 0$, low C; note that this condition applies as well at the interface against the seal layer during long-term quasi-static storage): Capillary forces control CO_2 invasion into the porous medium. Brine is the wetting phase and remains in the smaller pores. Capillary fingering may develop.

[51] Both viscous and capillary fingering patterns result in large irreducible saturation of the host fluid (brine). Oil-CO_2 phases behave differently to brine-CO_2 since part of the oil is miscible with CO_2 [*Blunt et al.*, 1993].

4.2. Sealing Capacity of Geological Formations

[52] The long-term storage of CO_2 is a quasi-static condition ($v = 0$, $C = 0$) controlled by capillary forces at pore

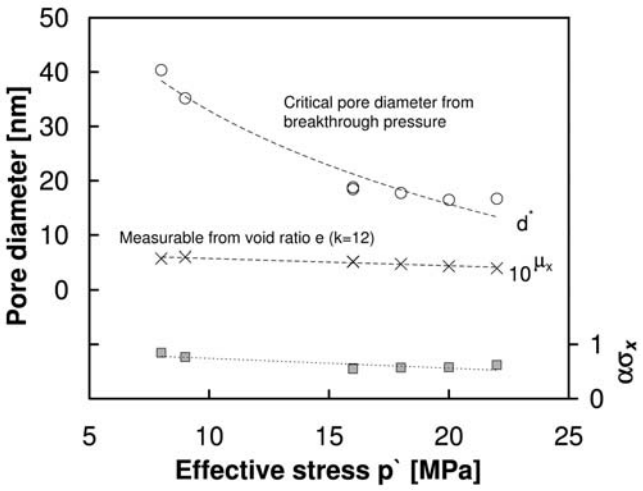

Figure 9. Critical pore diameter for gas breakthrough (equation (12)) and most prominent pore diameter as a function of effective stress in bentonite blocks (original data from the work of *Horseman et al.* [1999]). The secondary axis shows the factor $\alpha\sigma_x$ that quantifies the critical pore diameter d^* relative to the mean μ_x (equation (13)).

throats. The following analysis is conducted to identify the governing parameters and their interrelation.

[53] 1. Pore size distribution, mean value: Let us assume a lognormal distribution for pore size normalized by 1nm $x = \log(d/\text{nm})$ with mean μ_x = mean[log(d/nm)], standard deviation σ_x^2 = variance[log(d/nm)] and probability density function,

$$\text{Prob}(x) = \frac{1}{\sigma_x\sqrt{2\pi}}\exp\left(-\frac{(x-\mu_x)^2}{2\sigma_x^2}\right). \quad (9)$$

The mean μ_x can be extracted from mercury intrusion porosimetry [*Juang and Holtz*, 1986] or estimated theoretically as a function of the void ratio e, the specific surface S_s, and the mineral density ρ. For conglomerates made of edge-to-face and face-to-face aggregations of clay particles (geometric factor k between 6 and 12),

$$\mu_x = \log\left(\frac{k\,e}{S_s\rho}\frac{1}{\text{nm}}\right). \quad (10)$$

[54] 2. Void ratio and compressibility: The void ratio depends on the effective stress p' in agreement with Terzaghi's consolidation theory [*Burland*, 1990; *Terzaghi et al.*, 1996],

$$e = e_{1\text{ kPa}} - C_c\log\frac{p'}{1\text{ kPa}}, \quad (11)$$

where the void ratio $e_{1\text{ kPa}}$ at p' = 1 kPa and the compressibility coefficient of the sediment C_c increases with increasing specific surface.

[55] 3. Breakthrough pressure: For a given pore structure, there is breakthrough pressure P_c^* determined by the pressure-dependent interfacial tension σ and contact angle θ,

$$P_c^* = \frac{4\sigma\cos\theta}{d^*}, \quad (12)$$

where the critical pore size d^* is herein defined as the minimum pore size along a percolating path across the seal layer.

[56] 4. Critical pore size: The analysis of gas breakthrough experimental data from the works of *Hildenbrand et al.* [2002, 2004] and *Horseman et al.* [1999] indicates that $d^*/\text{nm} > 10^{\mu x}$; hence, the percolating path is made of pores all larger than the mean. The value of d^* can be related to the mean μ_x by a factor α of the standard deviation σ_x,

$$\log\left(\frac{d^*}{\text{nm}}\right) = \mu_x + \alpha\sigma_x. \quad (13)$$

Data from the work of *Horseman et al.* [1999] are analyzed using this formulation to estimate $\alpha\sigma_x$. We compute d^* from breakthrough (equation (12), water-helium interfacial properties from the work of *Hough et al.* [1952]) and μ_x from porosity (equation (10), mineral density and specific surface from the work of *Rosborg and Pan* [2008]). We obtain $\alpha\sigma_x = \log(d^*/\text{nm}) - \mu_x$. Results shown in Figure 9 indicate that $\alpha\sigma_x$ is relatively independent of effective stress, and it ranges between $\alpha\sigma_x = 0.7 \pm 0.15$ for this sediment (assumed geometric factor k = 12). Therefore, $d^*/\text{nm} = 10^{\mu_x+(0.7\pm0.15)}$.

[57] Finally, we can express the breakthrough pressure for an immiscible fluid as a function of effective stress p', sediment compressibility ($e_{1\text{ kPa}}$, C_c), pore structure (S_s, $\alpha\sigma_x$), and pressure-dependent interfacial tension σ and contact angle θ,

$$P_c^* = \psi\frac{S_s\rho\,\sigma\cos\theta}{e_{1\text{ kPa}} - C_c\log\dfrac{p'}{1\text{ kPa}}} \quad (\text{where } 0.04 \le \psi \le 0.08), \quad (14)$$

where the factor $\psi = 4/(k10^{\alpha\sigma x})$ groups theoretical and experimental constants and provides an order of magnitude estimation. Results in Figures 4 and 5 combine to make the wetting factor $\sigma\cos\theta$ a linearly decreasing function of pressure in either quartzitic and carbonate sediments, from $[\sigma\cos\theta] \approx 60$ mN/m at atmospheric pressure to $[\sigma\cos\theta] \approx 30$ mN/m on the L-V boundary. The wetting factor is very low for oil-wet sediments $[\sigma\cos\theta] < 5$ mN/m, and capillary forces vanish. Spontaneous imbibition takes place when $[\sigma\cos\theta] < 0$ mN/m. High values of breakthrough pressure are anticipated for clayey formations because of the high specific surface and small pore size; in this case, the presence of high-conductivity mesoscale features will define the geological plumbing and restrict storage capacity.

[58] Other concerns regarding CO_2 injection in geologic formations include change in surface charge of clays and associated double-layer effects due to decreased pore fluid pH [*Palomino and Santamarina*, 2005] and mineral dissolution and ensuing changes in effective stress leading to strain localization [*Shin et al.*, 2008] and increase in permeability [*Phillips*, 1991].

5. Conclusions

[59] Dissolved organic or inorganic species in water preferentially organize at the interface. Excess solute at the interface and the mass density of surrounding CO_2 determine interfacial tension. In particular, the interfacial tension between water and CO_2 decreases with pressure from ~65 ± 14 mN/m at atmospheric pressure to ~25 ± 7 mN/m beyond

the CO_2 V-L boundary. The variability in each case reflects solute type and concentration.

[60] Contact angle θ changes in agreement with Young-Dupre's equation. On hydrophobic substrates, the increase in contact angle θ with pressure can be as high as 60°. Oil-wet mineral surfaces may turn from hydrophilic at low gas pressure to hydrophobic at high gas pressure. There is a small decrease in contact angle on hydrophilic silica and calcite substrates.

[61] Water solubility in liquid CO_2 cannot be neglected when interparticle pendular water is involved. The effective diffusivity of water in liquid CO_2 is high $D = 1.5 \pm 0.3 \times 10^{-7}$ m^2/s ($D \sim 1.0 \times 10^{-7}$ for brine) primarily due to the low viscosity of liquid CO_2. This value is 2 orders of magnitude greater than diffusion values frequently invoked for ionic species in water.

[62] Pore water acidifies in the presence of CO_2 and can react with mineral substrates. Calcite dissolution, water diffusion in liquid CO_2, and calcite reprecipitation can take place in short-time scales (i.e., days) for pendular water between contacts.

[63] Capillary pressure and viscous forces play an important role in determining CO_2 injectability and the sealing capacity of geological formations. Two end-member scenarios can be identified: high-velocity viscosity-controlled flow (near injection wells) and quasi-static capillarity-controlled storage (far field and during long-term storage). Fingering and changes in imbibition patterns can develop.

[64] The breakthrough pressure is a function of sediment characteristics (primarily specific surface), overburden effective stress, and fluid pressure-dependent wetting conditions (interfacial tension and contact angle). The smallest pore size along a percolating path is larger than the mean pore diameter. It is anticipated that high-conductivity mesoscale paths will control the sealing capacity of clayey rocks.

Notation

σ_{fl} interfacial tension fluid-liquid, mN/m.
σ_{fs} interfacial tension fluid-solid, mN/m.
σ_{ls} interfacial tension liquid-solid, mN/m.
P pressure, MPa.
θ contact angle, degrees.
R_1, R_2 curvature radii, m.
ρ density, kg/m^3.
x, z Cartesian coordinates, m.
s curve length, m.
ϕ curve angle, rad.
ε error.
r radial coordinate, m.
t time, s.
D diffusion coefficient, m^2/s.
c solute concentration, mol/L, kg/M^3.
Γ surface excess of solute, mol/m^2.
T temperature, K.
μ viscosity, Pa·s.
v flow velocity, m/s.
M ratio between viscous forces.
C ratio between viscous and capillary forces.
d pore size, m.
x pore size normalized by 1nm.
e void ratio.
S_s specific surface, m^2/kg.
p' confinement, Pa.
C_c compressibility coefficient of the sediment.
P_c^* breakthrough pressure, Pa.

[65] **Acknowledgments.** Support for this research was provided by the U. S. Department of Energy and the Goizueta Foundation. Any opinions, findings, conclusions, or recommendations expressed herein are those of the authors and do not necessarily reflect the views of funding organizations. We are grateful to the anonymous reviewers for insightful comments and suggestions.

References

Bhatt, D., et al. (2004), Molecular dynamics simulations of surface tensions of aqueous electrolytic solutions, *J. Phys. Chem. B*, *108*(26), 9077–9084.
Blokhuis, E. M. (2004), Liquid drops at surfaces, in *Surface and Interfacial Tension: Measurement, Theory, and Applications*, edited by S. Hartland, p. 619, Marcel Dekker, New York.
Blunt, M., et al. (1993), Carbon-dioxide in enhanced oil-recovery, *Energy Convers. Manage.*, *34*, 1197–1204.
Bryar, T. R., and R. J. Knight (2003), Laboratory studies of the effect of sorbed oil on proton nuclear magnetic resonance, *Geophysics*, *68*(3), 942–948.
Burland, J. B. (1990), On the Compressibility and Shear Strength of Natural Clays, *Geotechnique*, *40*, 329–378.
Butt, H.-J., et al. (2006), *Physics and Chemistry of Interfaces*, 2nd, revised and enlarged edition, Wiley- VCH Verlag GmbH & Co. KGaA, Weinheim.
Canny, J. (1986), A computational approach to edge-detection, *IEEE Trans. Pattern Anal.*, *8*, 679–698, doi:10.1109/TPAMI.1986.4767851.
Chalbaud, C., et al. (2009), Interfacial tension measurements and wettability evaluation for geological CO_2 storage, *Adv. Water Resour.*, *32*, 98–109.
Chi, S. M., et al. (1988), Study of interfacial properties in the liquid CO_2 water coal system, *Energy Fuels*, *2*, 141–145.
Chiquet, P., et al. (2007), Wettability alteration of caprock minerals by carbon dioxide, *Geofluids*, *7*, 112–122.
Chrastil, J. (1982), Solubility of solids and liquids in supercritical gases, *J. Phys. Chem.*, *86*, 3016–3021.
Chun, B.-S., and G. T. Wilkinson (1995), Interfacial tension in high-pressure carbon dioxide mixtures, *Ind. Eng. Chem. Res.*, *34*, 4371–4377.
Cowan, J. C., and D. J. Weintritt (1976), *Water-Formed Scale Deposits*, Gulf Publishing Co., Houston, Texas.
Danten, Y., et al. (2005), Dynamic of solitary water in hydrophobic solvents, *J. Mol. Liq.*, *117*, 49–61.
da Rocha, S. R. P., et al. (2001), Molecular structure of the water-supercritical CO_2 interface, *J. Phys. Chem. B*, *105*(48), 12,092–12,104.
Decker, E. L., et al. (1999), Physics of contact angle measurement, *Colloids Surf. A.*, *156*, 177–189.
Defay, R., and I. Prigogine (1966), *Surface Tension and Adsorption*, 432 pp., Wiley, New York.
Dickson, J. L., et al. (2006), Wetting phenomena at the CO_2/water/glass interface, *Langmuir*, *22*, 2161–2170.
Drever, J. I. (1997), *The Geochemistry of Natural Waters: Surface and Groundwater Environments. Third Edition*, 437 pp., Prentice-Hall, New Jersey.
Duan, Z., and R. Sun (2003), An improved model calculating CO2 solubility in pure water and aqueous NaCl solutions from 273 to 533K and from 0 to 2000 bar, *Chem. Geol.*, *193*(3–4), 257–271.
Fenghour, A., et al. (1998), The viscosity of carbon dioxide, *J. Phys. Chem. Ref. Data*, *27*, 31–44.
Funazukuri, T., et al. (1992), Predictive correlation for binary diffusion-coefficients in dense carbon-dioxide, *AIChE J.*, *38*, 1761–1768.
Hildenbrand, A., et al. (2002), Gas breakthrough experiments on fine-grained sedimentary rocks, *Geofluids*, *2*(1), 3–23.
Hildenbrand, A., et al. (2004), Gas breakthrough experiments on pelitic rocks: Comparative study with N-2, CO2 and CH4, *Geofluids*, *4*, 61–80.
Horseman, S. T., et al. (1999), Gas migration in clay barriers, *Eng. Geol.*, *54*, 139–149.
Hough, E. W., et al. (1952), Adsorption at water-helium water-methane and water-nitrogen interfaces at pressures to 15,000 psia, *J. Phys. Chem.*, *56*, 996–999.
Jackson, K., et al. (1995), Water solubility measurements in supercritical fluids and high-pressure liquids using near-infrared spectroscopy, *Anal. Chem.*, *67*, 2368–2372.

Johnson, J. W., et al. (1992), SUPCRT92: A software package for calculating the standard molal thermodynamic properties of minerals, gases, aqueous species, and reactions from 1 to 5000 bar and 0 to 1000°C, *Comp. Geosci.*, *18*, 899–947.

Juang, C. H., and R. D. Holtz (1986), A probabilistic permeability model and the pore size density function, *Int. J. Numer. Anal. Met.*, *10*, 543–553, doi:510.1002/nag.1610100506.

Krynicki, K., et al. (1978), Pressure and temperature-dependence of self-diffusion in water, *Faraday Discuss.*, *66*, 199–208, doi:110.1039/DC9786600199.

Kuznetsova, T., and B. Kvamme (2002), Thermodynamic properties and interfacial tension of a model water-carbon dioxide system, *Phys. Chem. Chem. Phys.*, *4*(6), 937–941.

Kvamme, B., et al. (2007), Measurements and modelling of interfacial tension for water plus carbon dioxide systems at elevated pressures, *Comput. Mater. Sci.*, *38*, 506–513.

Lenormand, R., et al. (1988), Numerical-models and experiments on immiscible displacements in porous-media, *J. Fluid Mech.*, *189*, 165–187, doi:110.1017/S0022112088000953.

Liong, K. K., et al. (1992), Diffusion of fatty-acid esters in supercritical carbon-dioxide, *Ind. Eng. Chem. Res.*, *31*, 390–399.

Massoudi, R., and A. D. King (1974a), Effect of pressure on surface-tension of water - adsorption of low-molecular weight gases on water at 25 degrees, *J. Phys. Chem.*, *78*, 2262–2266.

Massoudi, R., and A. D. King (1974b), Effect of pressure on interfacial-tension of aqueous-solutions in equilibrium with compressed gases, *Abs. Pap. Am. Chem. Soc.*, 179–179.

McCutcheon, S. C., et al. (1993), Water quality, in *Handbood of Hydrology*, edited by D. R. Maidment, McGraw-Hill, New York.

Montes-Hernandez, G., et al. (2007), Calcite precipitation from CO_2-H_2O-$Ca(OH)_2$ slurry under high pressure of CO_2, *J. Cryst. Growth*, *308*, 228–236.

Netherton, R., et al. (1977), Viscosity of brine from Salton sea geothermal field, California, from 25-degrees-C to 90-degrees-C at 100 kPa, *Trans. AGU*, *58*, 1248–1248.

Palomino, A. M., and J. C. Santamarina (2005), Fabric map for kaolinite: Effects of pH and ionic concentration on behavior, *Clay Clay Min.*, *53*, 211–223.

Pegram, L. M., and M. T. Record (2007), Hofmeister salt effects on surface tension arise from partitioning of anions and cations between bulk water and the air-water interface, *J. Phys. Chem. B*, *111*, 5411–5417.

Pennell, K. D., et al. (1996), Influence of viscous and buoyancy forces on the mobilization of residual tetrachloroethylene during surfactant flushing, *Environ. Sci. Technol.*, *30*, 1328–1335.

Perry, R., and D. Green (1997), *Perry's Chemical Engineering Handbook*, 7th ed., McGraw-Hill, New York.

Phillips, O. M. (1991), *Flow and Reactions in Permeable Rocks*, Cambridge Univ. Press.

Plug, W. J., and J. Bruining (2007), Capillary pressure for the sand-CO_2-water system under various pressure conditions. Application to CO_2 sequestration, *Adv. Water Resour.*, *30*, 2339–2353.

Pope, G. A., and M. Baviere (1991), Reduction of capillary forces by surfactants, in *Basic Concepts in Enhanced Oil Recovery Processes*, edited by M. Baviere, Elsevier Applied Science, London.

Rosborg, B., and J. Pan (2008), An electrochemical impedance spectroscopy study of copper in a bentonite/saline groundwater environment, *Electrochim. Acta*, *53*, 7556–7564.

Rosen, M. J., et al. (2005), Ultralow interfacial tension for enhanced oil recovery at very low surfactant concentrations, *Langmuir*, *21*, 3749–3756.

Rotenberg, Y., et al. (1983), Determination of surface tension and contact angle from the shapes of axisymmetric fluid interfaces, *J. Colloid Int. Sci.*, *93*, 169–183.

Sabirzyanov, A. N., et al. (2002), Solubility of water in Supercritical carbon dioxide, *High Temp.*, *40*(2), 203–206.

Sassiat, P. R., et al. (1987), Measurement of diffusion-coefficients in supercritical carbon-dioxide and correlation with the equation of Wilke and Chang, *Anal. Chem.*, *59*, 1164–1170.

Seo, Y., et al. (2002), Methane and carbon dioxide hydrate phase behavior in small porous silica gels: Three-phase equilibrium determination and thermodynamic modeling, *Langmuir*, *18*(24), 9164–9170.

Sharma, H. D., and K. R. Reddy (2001), *Geoenvironmental Engineering: Site Remediation, Waste Containment, and Emerging Waste Management Technologies*, John Wiley & Sons, Inc., Hoboken, New Jersey.

Shin, H., et al. (2008), Contraction-driven shear failure in compacting uncemented sediments, *Geology*, *36*, 931–934.

Siemons, N., et al. (2006), Pressure dependence of the contact angle in a CO_2-H_2O-coal system, *J. Colloid Int. Sci.*, *297*, 755–761.

Spycher, N., et al. (2003), CO_2-H_2O mixtures in the geological sequestration of CO_2. I. Assessment and calculation of mutual solubilities from 12 to 100°C and up to 600 bar, *Geochim. Cosmochim. Acta*, *67*(16), 3015–3031.

Stumm, W., and J. J. Morgan (1996), *Aquatic Chemistry: Chemical Equilibria and Rates in Natural Waters*, 3rd ed., JohnWiley & Sons, Inc., New York.

Suarez-Iglesias, O., et al. (2008), Limiting diffusion coefficients of ethyl benzoate, benzylacetone, and eugenol in carbon dioxide at supercritical conditions, *J. Chem. Eng. Data*, *53*, 779–784.

Suekane, T., et al. (2009), Application of MRI in the measurement of two-phase flow of supercritical CO_2 and water in porous rocks, *J. Porous Media*, *12*, 143–154.

Sun, C. Y., et al. (2004), Interfacial tension of methane plus water with surfactant near the hydrate formation conditions, *J. Chem. Eng. Data*, *49*, 1023–1025.

Sutjiadi-Sia, Y., et al. (2007), The effect of in liquids dissolved dense gases on interfacial and wetting characteristics, *Forsch. Ingenieurwes.*, *71*, 29–45.

Sutjiadi-Sia, Y., et al. (2008), Interfacial tension of solid materials against dense carbon dioxide, *J. Colloid Int. Sci.*, *320*, 268–274.

Terzaghi, K., et al. (1996), *Soil Mechanics in Engineering Practice*, 3rd ed., 549 pp., John Wiley & Sons, New York.

Thomas, W. J., and M. J. Adams (1965), Measurement of diffusion coefficients of carbon dioxide and nitrous oxide in water and aqueous solutions of glycerol, *Trans. Faraday Soc.*, *61*, 668–673.

Tuckermann, R. (2007), Surface tension of aqueous solutions of water-soluble organic and inorganic compounds, *Atmos. Environ.*, *41*, 6265–6275.

Watanabe, K., et al. (2005), Surfactant effects on hydrate formation in an unstirred gas/liquid system: An experimental study using HFC-32 and sodium dodecyl sulfate, *Chem. Eng. Sci.*, *60*, 4846–4857.

Wiebe, R. (1941), The binary system carbon dioxide-water under pressure, *Chem. Rev.*, *29*, 475–481.

Xu, B., et al. (2003), Diffusion of water in liquid and supercritical carbon dioxide: An NMR study, *J. Phys. Chem. A*, *107*(1), 1–3.

D. N. Espinoza and J. C. Santamarina, School of Civil and Environmental Engineering, Georgia Institute of Technology, 790 Atlantic Dr., Atlanta, GA 30332-0355, USA. (nicolas@ce.gatech.edu; jcs@gatech.edu)